energies

MDPI

Article

Study of a Bidirectional Power Converter Integrated with Battery/Ultracapacitor Dual-Energy Storage

Ching-Ming Lai [1], Jiashen Teh [2,*], Yuan-Chih Lin [3] and Yitao Liu [4,*]

[1] Department of Electrical Engineering, National Chung Hsing University, Taichung 420, Taiwan; pecmlai@gmail.com
[2] School of Electrical and Electronic Engineering, Engineering Campus, Universiti Sains Malaysia (USM), Nibong Tebal 14300, Penang, Malaysia
[3] Department of Electrical Engineering, National Taiwan University, Taipei 106, Taiwan; gero.lin1980@gmail.com
[4] College of Mechatronics and Control Engineering, Shenzhen University, Shenzhen 518060, China
* Correspondence: jiashenteh@usm.my (J.T.); liuyt@szu.edu.cn (Y.L.)

Received: 31 January 2020; Accepted: 1 March 2020; Published: 6 March 2020

Abstract: A patented bidirectional power converter was studied as an interface to connect the DC-bus of driving inverter, battery energy storage (BES), and ultracapacitor (UC) to solve the problem that the driving motor damages the battery life during acceleration and deceleration in electric vehicles (EVs). The proposed concept was to adopt a multiport switch to control the power flow and achieve the different operating mode transitions for the better utilization of energy. In addition, in order to improve the conversion efficiency, the proposed converter used a coupled inductor and interleaved-pulse-width-modulation (IPWM) control to achieve a high voltage conversion ratio (i.e., bidirectional high step-up/down conversion characteristics). This study discussed the steady-state operation and characteristic analysis of the proposed converter. Finally, a 500 W power converter prototype with specifications of 72 V DC-bus, 24 V BES, and 48 V UC was built, and the feasibility was verified by simulation and experiment results. The highest efficiency points of the realized prototype were 97.4%, 95.5%, 97.2%, 97.1%, and 95.3% for the UC charge, battery charge, UC discharge, the dual-energy in series discharge, and battery discharge modes, respectively.

Keywords: battery/ultracapacitor; dual-energy; bidirectional power converter; electric vehicles

1. Introduction

Electric vehicle (EV) technologies are currently being developed to lessen environmental impact and overcome shortages of fossil fuel [1–10]. The typical power configuration of pure electric vehicle (EV) contains four major parts: the battery energy storage (BES), the power converter, the driving inverter of motor, and the energy management system (EMS) [6,8,10]. Among them, BES is the most critical component, which can directly affect the life and endurance of the EV, driving efficiency, and system performance. In general, the power will be drawn rapidly from the BES during the vehicle acceleration, subsequently causing BES output current and temperature to rise quickly. Moreover, the driving inverter is prone to generate less stable pulse currents for the BES during deceleration [9]. Such long-term use not only causes damage to the external body of the battery but also excessively charges and discharges the BES, which eventually will shorten the lifespan of the BES, specifically in high power applications. Although it is feasible to size up the BES for high power demands, the high price of the overall system still remains an issue. Possible solutions may be to select an ultracapacitor (UC), to assist BES, forming a "hybrid energy" system as shown in Figure 1 for EVs [11,12].

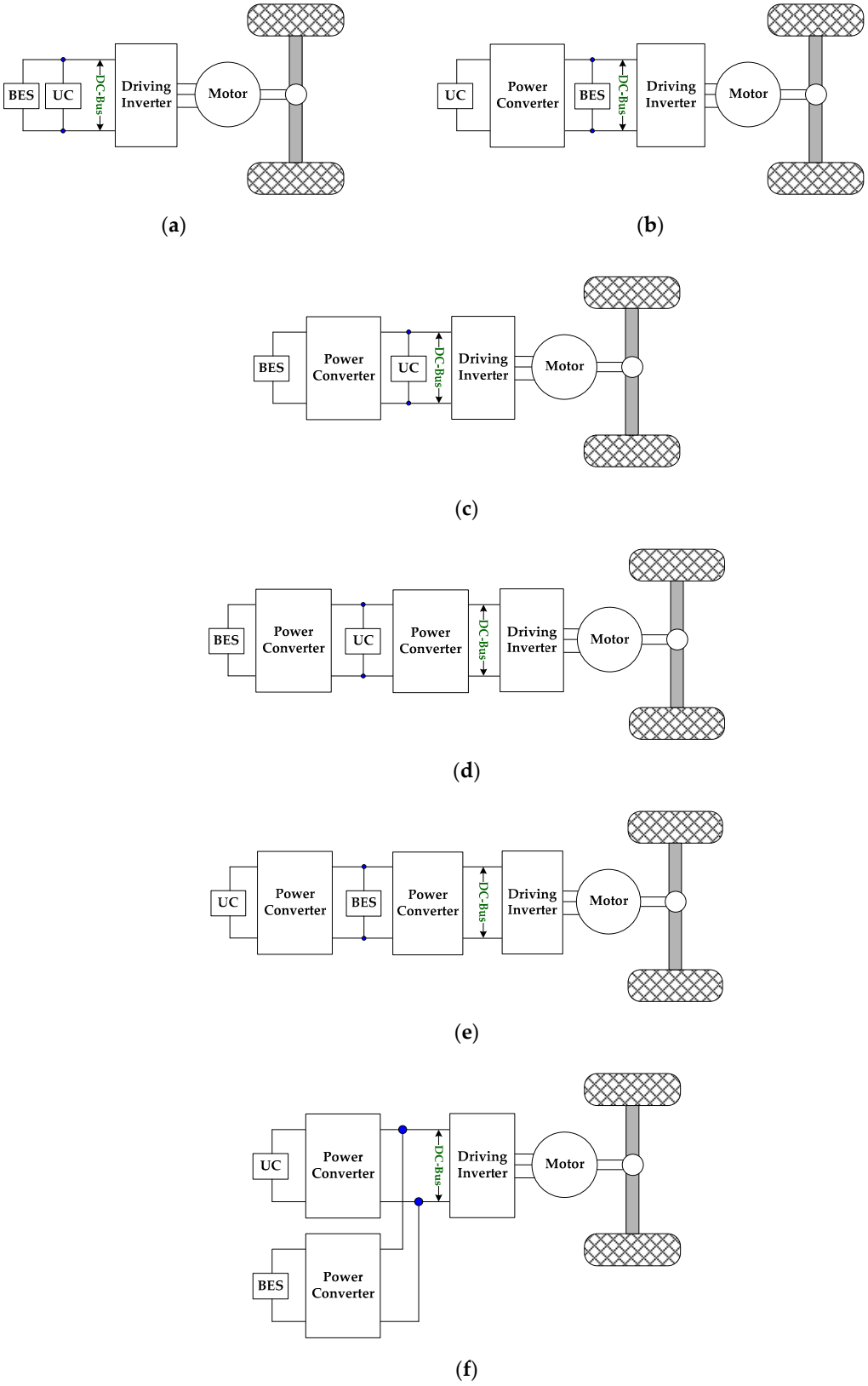

Figure 1. Several schemes of interfacing battery energy storage (BES) and ultracapacitor (UC) to the DC-bus in electric vehicle (EV) power train: (**a**) Directly parallel hybrid scheme; (**b**) UC/BES scheme; (**c**) BES/UC scheme; (**d**) type-I of cascaded scheme; (**e**) type-II of cascaded scheme; (**f**) multiple converter parallel scheme.

UC has high-power density, long cycle life, quick dynamic response, but low-energy-density, which are opposite toward BES. Hence, it should exploit the complementary properties of both the UC and the BES [12]. Several conventional schemes integrating both the BES and UC are shown in Figure 1. These schemes have all been designed to control power flows, supply specific voltages to loads, and to reduce design cost, mass, and power consumptions [12–15].

Figure 1a shows the most basic parallel scheme of the BES and UC, with the latter serving as the low-pass filter [16]. Although simple, the energy stored in the UC is not utilized effectively due to the absence of power converters. The slightly more robust Figure 1b shows that a power converter is added in between the BES and UC [17–20]. In this scheme, the BES is connected directly to the DC-bus instead of the UC. The power output of the UC is controlled by the power converter, and this enables the UC to operate over a wider voltage range than in Figure 1a. Due to this, the power rating of the converter has to be sufficiently large to handle high surges of power demands from the UC. The purpose of the power converter is also to maintain a constant voltage value on the DC-bus during the operation of the motor. The drawback of this scheme is that the BES is exposed to large fluctuations of high charging and discharging current, resulting in its reduced lifetime. Figure 1c is similar to Figure 1b except that the positions of the BES and UC have been swapped [21]. Due to this, the BES is no longer exposed to the large current fluctuations. The power output from the BES is now controlled by the power converter. The main disadvantage of this scheme is that the DC-bus voltage is exposed to large voltages as it is directly connected to the UC. As a result, the power converter is exposed to a high risk of suffering adverse losses, especially in harsh driving conditions.

All the schemes in Figure 1a–c clearly demonstrate that it is insufficient to use only one or no power converter. Hence, cascaded schemes using two power converters, as shown in Figure 1d,e, have also been considered before [22,23]. In these two schemes, two converters decouple the BES and UC from the DC-bus. The circuit, in Figure 1d, is also known as the "type-I scheme" where an extra power converter is added in between the UC and the DC-bus. The converter that is located in between the BES and UC is rated according to the power rating of the BES. This scheme creates more losses for the higher rated converter that is located in between the UC and the DC-bus due to the fluctuations of the UC output voltage. In order to overcome this problem, the positions of the BES and UC are swapped, as shown in Figure 1e (type-II scheme). However, it is difficult to balance the BES cell due to it now being located at the higher voltage terminal. Although both the type-I and type-II schemes are more robust than all the previous designs that use only one or no power converter, the power losses and design costs of the schemes are increased substantially owing to the multi-stage energy conversion processes in the vehicular power train. Besides that, only one power converter is connected to the DC-bus in both of these schemes. An outage in one of the power converters will lead to the loss of the power-control function. An alternative is to employ the scheme in Figure 1f, where the power converters are connected in parallel and directly to the DC-bus [13,24–28]. In this scheme, the power converters have the same output voltage, and the power flow of both the energy sources (BES and UC) are not affected by the output of the other converter. Consequently, this scheme can operate in various modes [28]. But, the fully power-rated converters are needed, and the cost of this scheme is higher than all the aforementioned schemes.

In order to reduce the overall system cost, a multi-input power converter scheme is studied, as shown in Figure 2, into the EV system [29–33].

Multi-input power converters are potential solutions when multiple energy sources with different voltage levels (battery voltage ≠ UC voltage ≠ DC-bus voltage) and/or power capabilities are to be combined and yet maintain a regulated output load voltage across them.

Using multi-input power converters, it is possible to apply a different power control command for each input source. In order to reduce the cost and weight and enhance the overall performance of the hybrid energy storage system, the multi-input power converter scheme was chosen in this paper and further investigated.

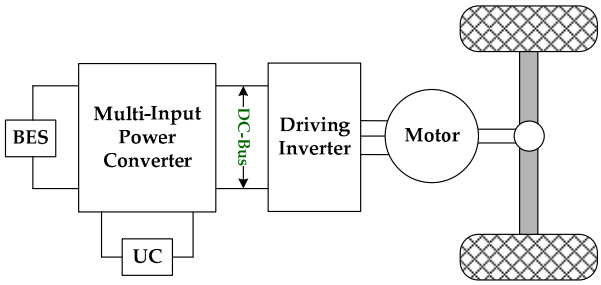

Figure 2. Multi-input power converter interfacing BES and UC to the DC-bus in the EV power train.

In [29], a multi-input power converter topology has been proposed to combine various input energy sources in parallel by using a single-pole triple-throw switch. The major limitations of parallel-connected source topologies are: input source voltage should be asymmetric, and only one input source can supply power to the load at a time to avoid the power coupling effect.

In [30], a single-inductor unidirectional multi-input power converter has been presented, which can operate in buck, boost, or buck-boost modes. To realize the bidirectional power flow mode, all the diodes must be replaced by unidirectional switches, which increase the number of switches.

In [31], a DC-bus interfacing three-port converter with a simple topology and no electrical isolation has been proposed, but it cannot cope with a wide operating voltage ratio; energy storage devices connected to different ports must have a similar operating voltage, and this constricts the application.

In [32], a modular multi-input power converter has been presented to integrate the basic buck-boost circuit and a shared DC-bus. It is a very simple approach to integrate multiple converters into a single unit. However, it has limited static voltage gains, resulting in a narrow voltage range and a low voltage difference between the high- and low-side ports. Besides, since only a few circuit elements are shared among multiple converters, the benefits of the integration are limited.

In [33], a two-phase multi-input converter with a high voltage conversion ratio has been proposed as an interface between dual-energy storage sources. Due to the intrinsic automatic current balance characteristic, the currents of two energy sources are theoretically identical; it indicates that the high power capability of UC cannot be utilized, and the applications of the proposed converter would be limited.

By conducting a research literature review of [29–36], in this paper, a bidirectional power converter integrated BES/UC dual-energy storage was proposed, which had the capability to perform forward power transmission and reverse energy recovery.

First, the proposed converter used a multiport switch to change the different operating modes and to improve the energy utilization of UC and increase battery life.

Second, it was also integrated with interleaved-pulse-width-modulation (IPWM) control to increase power density and reduce bidirectional current ripples, which makes power delivery more reliable.

Third, the proposed converter also used a coupled inductor technique instead of a general single-winding inductor to achieve high voltage conversion ratio and high power density for bidirectional power conversion.

Finally, the steady-state operation and characteristic analysis of the proposed converter were described, validated using simulation and experimentation of a 500 W power converter prototype with specifications of 72 V DC-bus, 24 V BES, and 48 V UC.

The summarized main features of the proposed converter were its ability to:

(1) interface more than two energy sources of different voltage levels,
(2) control power flow between the DC-bus and the two low-voltage energy sources,
(3) control power flow from either the UC or BES or both,
(4) enhance static voltage gain and reduce switch voltage stress, and
(5) possess a reasonable duty cycle and produce a wide voltage difference between its high- and low-side ports.

2. Converter Operating Principles

Figure 3 shows the architecture of the proposed converter integrated with dual-energy storage. The power devices (S_1~S_4) are the multiport switch used to control the power flow between the battery/UC dual-energy and DC-bus. To achieve the high conversion efficiency, the design concept for the converter are based on multi-phase operation and switch stress reduction as (1) the power devices (Q_1~Q_4) are designed to use IPWM control to reduce current stress and ripple on the switch, (2) two-phase coupled inductors T_1 and T_2 are integrated into the bidirectional power converter with high turns ratio to reduce the undesirable duty ratio and conduction loss of metal-oxide-semiconductor field-effect transistors (MOSFETs).

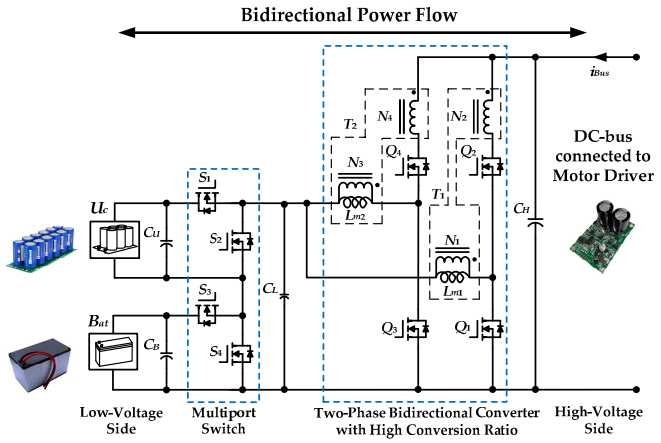

Figure 3. The proposed bidirectional power converter architecture.

2.1. Multiport Switch

Figure 4 shows the equivalent circuits of the multiport switch of the proposed converter under different operating modes. For the converter operating in the UC charge or discharge mode, the multiport switches S_1, S_4 are turned on, and S_2, S_3 are turned off. The equivalent circuit of this condition is shown in Figure 4a. It is shown that the bidirectional energy delivery between the UC and the DC-bus can be achieved. For the converter operating under the battery charge mode or discharge mode, the multiport switches S_2, S_3 are turned on, and S_1, S_4 are turned off. Under this condition, the corresponding equivalent circuit is shown in Figure 4b. The figure shows that the bidirectional energy delivery between the battery and the DC-bus can be achieved. For the converter operating under the dual-energy in series discharge mode, the multiport switches S_1, S_3 are turned on, and S_2, S_4 are turned off. The battery/UC dual-energy delivers the energy to DC-bus, and its equivalent circuit is shown in Figure 4c.

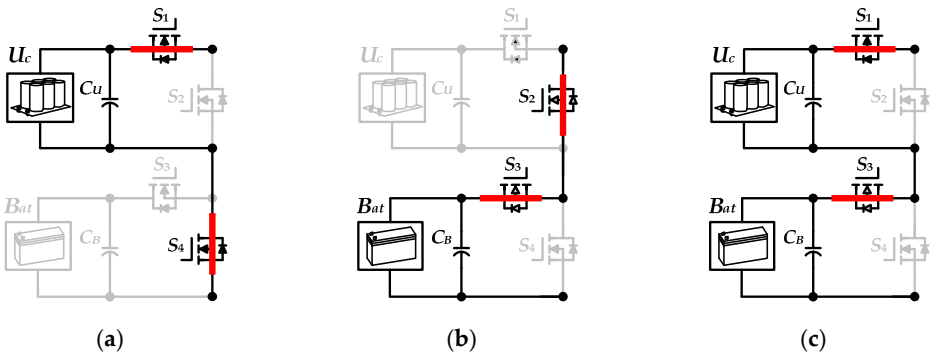

Figure 4. Equivalent circuits of the multiport switch under different operating modes. (**a**) UC charge mode or discharge mode. (**b**) Battery charge mode or discharge mode. (**c**) Battery/UC dual-energy in series discharge mode.

2.2. Operating Principle of the Proposed Converter

Figure 5 shows the equivalent circuits of the different states for the proposed converter, where V_H represents the high-side voltage for the DC-bus, and V_L represents low-side voltage for UC, battery, or battery/UC dual-energy in series modes.

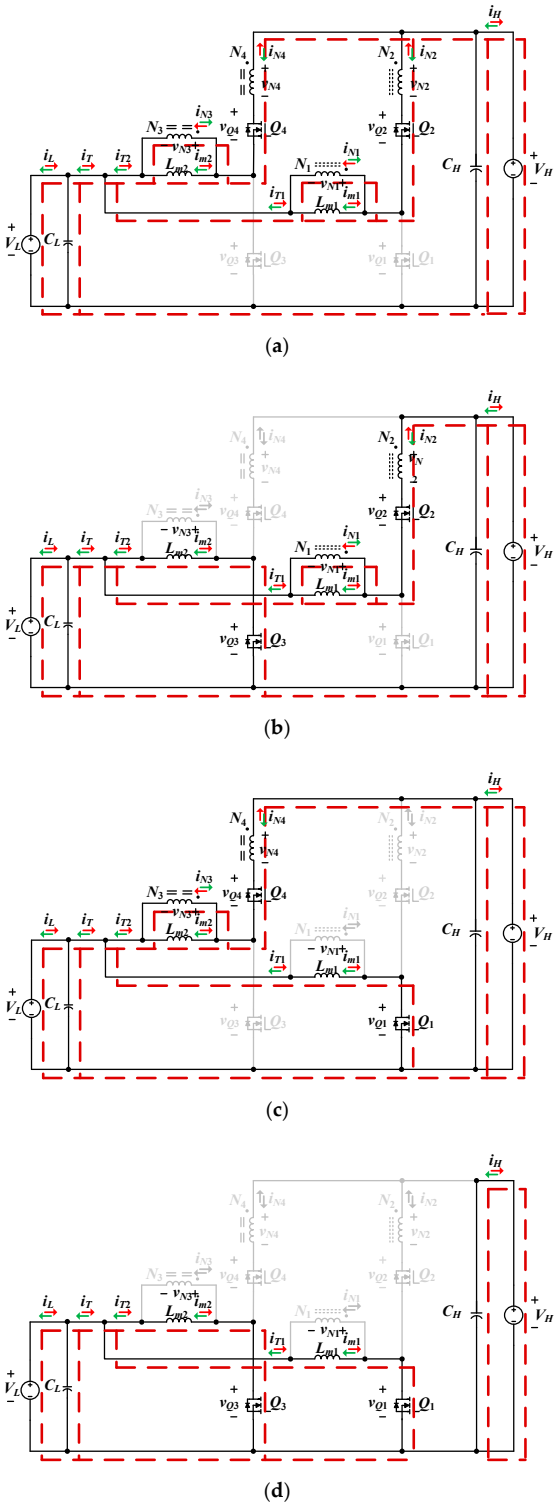

Figure 5. Equivalent circuits of the proposed converter. (**a**) State 1: Q_2, Q_4 on, and Q_1, Q_3 off. (**b**) State 2: Q_2, Q_3 on, and Q_1, Q_4 off. (**c**) State 3: Q_1, Q_4 on, and Q_2, Q_3 off. (**d**) State 4: Q_1, Q_3 on, and Q_2, Q_4 off. (The arrows in **green** indicate the charge mode, and the arrows in **red** indicate the discharge mode.).

The assumptions are made in analyzing the proposed converter:

(1) the converter operates in continuous conduction mode (CCM);
(2) characteristic of the two-phase coupled inductors T_1 and T_2 are the same, i.e., $L_{m1} = L_{m2}$, $i_{m1} = i_{m2}$ and $n = N_2/N_1 = N_4/N_3$;
(3) all voltages and currents in the circuits are periodic in steady-state condition; for simplicity, it is assumed that all the components in Figure 3 are idealized.

State 1. The equivalent circuit of this state is shown in Figure 5a. The power switches Q_2 and Q_4 are turned on, and Q_1 and Q_3 are turned off. During this state, the high-side voltage V_H stores energy to the magnetizing inductance L_{m1} and L_{m2}, and then the magnetizing currents i_{m1}, i_{m2} increase linearly. The circuit equations are expressed as follows,

$$v_{N1} = L_{m1}\frac{di_{m1}}{dt} = V_H - v_{N2} - V_L \tag{1}$$

$$v_{N3} = L_{m2}\frac{di_{m2}}{dt} = V_H - v_{N4} - V_L \tag{2}$$

$$i_H = i_{N2} + i_{N4} \tag{3}$$

$$i_{T1} = i_{N2} \tag{4}$$

$$i_{T2} = i_{N4} \tag{5}$$

$$i_T = i_{T1} + i_{T2} \tag{6}$$

State 2. The equivalent circuit of this state is shown in Figure 5b. The power switches Q_2 and Q_3 are turned on, and Q_1 and Q_4 are turned off. At this time, the high-side voltage V_H continues to store energy to the magnetizing inductance L_{m1}, and the magnetizing current i_{m1} increases linearly. The energy stored in the magnetizing inductor L_{m2} is now released to the low-side energy device, and the magnetizing current i_{m2} decreases linearly. The circuit equations are expressed as follows,

$$v_{N1} = V_H - v_{N2} - V_L \tag{7}$$

$$v_{N3} = -V_L \tag{8}$$

$$i_H = i_{N2} \tag{9}$$

$$i_{T1} = i_{N2} \tag{10}$$

$$i_{T2} = i_{m2} \tag{11}$$

State 3. The equivalent circuit of this state is shown in Figure 5c. The power switches Q_1 and Q_4 are turned on, and Q_2 and Q_3 are turned off. At this time, the energy stored in the magnetizing inductor L_{m1} is now released to the low-side energy storage, and the magnetizing current i_{m1} decreases linearly. The voltage across v_{N1} of the magnetizing inductor L_{m1} is negative of the low-side voltage V_L. The magnetizing inductor L_{m2} draws the energy from the high-side voltage V_H, and the magnetizing current i_{m2} increases linearly. The circuit equations are expressed as follows,

$$v_{N1} = -V_L \tag{12}$$

$$v_{N3} = V_H - v_{N4} - V_L \tag{13}$$

$$i_H = i_{N4} \tag{14}$$

$$i_{T1} = i_{m1} \tag{15}$$

$$i_{T2} = i_{N4}. \tag{16}$$

State 4. The equivalent circuit of this state is shown in Figure 5d. The power switches Q_1 and Q_3 are turned on, and Q_2 and Q_4 are turned off. At this time, the energy stored in the magnetizing inductor L_{m1} and L_{m2} is now released to the low-side energy storage, and the magnetizing currents i_{m1} and i_{m2} decrease linearly. The voltage across v_{N1} and v_{N3} of the magnetizing inductor L_{m1} and L_{m2} is negative of the low-side voltage V_L. The circuit equations are expressed as follows,

$$v_{N1} = -V_L \tag{17}$$

$$v_{N3} = -V_L \tag{18}$$

$$i_H = 0 \tag{19}$$

$$i_{T1} = i_{m1} \tag{20}$$

$$i_{T2} = i_{m2} \tag{21}$$

Considering the different duty ratio conditions in the charge mode and discharge mode, the operating state flow of each condition during a switching period is summarized as follows.

Charge Mode (D_c < 0.5)

State 2 → State 4 → State 3 → State 4

Charge Mode (D_c = 0.5)

State 2 → State 3

Charge Mode (D_c > 0.5)

State 2 → State 1 → State 3 → State 1

Discharge Mode (D_d < 0.5)

State 3 → State 1 → State 2 → State 1

Discharge Mode (D_d = 0.5)

State 3 → State 2

Discharge Mode (D_d > 0.5)

State 3 → State 4 → State 2 → State 4

As mentioned above, D_c is the duty ratio of switch Q_2 and Q_4 for the charge mode, and D_d is the duty ratio of switch Q_1 and Q_3 for the discharge mode.

When the proposed converter operates with the duty ratio of 0.5 in the charge or discharge mode (i.e., $D_c = D_d = 0.5$), the only two operating states of the proposed converter are produced.

When the proposed converter operates in the charge mode with duty ratio $D_c > 0.5$, the operation state in a switching period is the same as the discharge mode with $D_d < 0.5$, and only the reverse current direction is considered.

Similarly, when the proposed converter operates in the discharge mode with the duty ratio $D_d > 0.5$, the operation state in the switching period is the same as the charge mode with $D_c < 0.5$, and only the reverse current direction is considered. Figure 6 shows the key waveforms of the proposed converter in the charge mode with $D_c < 0.5$, and in the discharge mode with $D_d < 0.5$, respectively.

The time intervals of Figure 6 are described as

Charge Mode (D_c < 0.5)

$[t_0 < t \le t_1]$: state 2; $[t_1 < t \le t_2]$: state 4; $[t_2 < t \le t_3]$: state 3; $[t_3 < t \le t_4]$: state 4.

Discharge Mode (D_d < 0.5)

$[t_0 < t \le t_1]$: state 3; $[t_1 < t \le t_2]$: state 1; $[t_2 < t \le t_3]$: state 2; $[t_3 < t \le t_4]$: state 1.

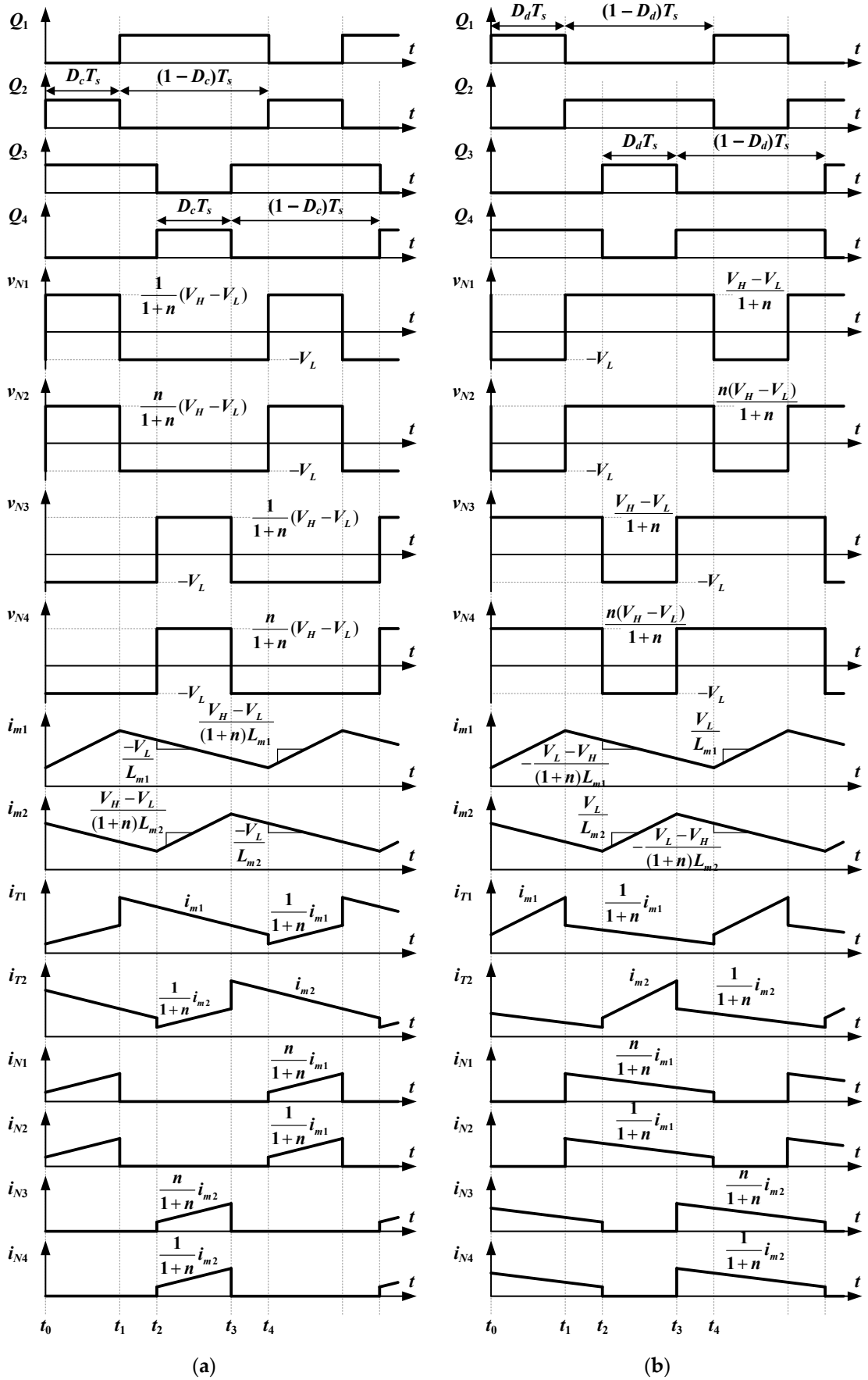

Figure 6. Key waveforms: (**a**) charge mode and $D_c < 0.5$; (**b**) discharge mode and $D_d < 0.5$.

3. Converter Steady-State Analyses

3.1. Static Voltage Conversion Ratio Analysis

Charge Mode (UC Charge; Battery Charge)

During steady-state operation and according to the volt-second balance principle of the magnetizing inductance operating in the charge mode, the static voltage conversion ratio M_c can be derived as from (22)–(25).

The voltage relationship between primary and secondary sides of the coupled inductor is shown as follows

$$v_{N2} = nv_{N1} \tag{22}$$

substituting (22) into (1), it can be rewritten as follows

$$v_{N1} = (V_H - V_L)\frac{1}{1+n} \tag{23}$$

By combining (23) and (12), the average voltage of the primary side for the coupled inductor during a switching period can be expressed as follows

$$\langle v_{N1} \rangle_{T_s} = \int_0^{D_c T_s} \frac{V_H - V_L}{1+n} dt + \int_{D_c T_s}^{T_s} (-V_L) dt = 0 \tag{24}$$

The static voltage conversion ratio of the proposed converter in the charge mode can be derived as follows

$$M_c = \frac{V_L}{V_H} = \frac{D_c}{1+n(1-D_c)} \tag{25}$$

Figure 7a shows the relationship between the coupled inductance with different turns ratio and the static voltage conversion ratio M_c of the proposed converter in the charge mode.

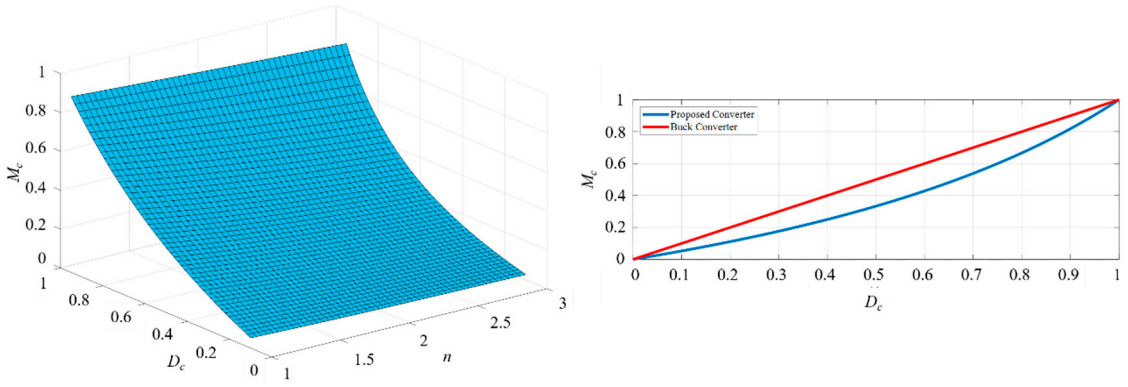

(**a**) (**b**)

Figure 7. Converter characteristics in charge mode: (**a**) relationship diagram of M_c, D_c, and n; (**b**) relationship diagram of M_c and D_c (n = 1).

For simplicity, assuming that the turns ratio of the coupling inductance is n = 1, the relationship between M_c and D_c is shown in Figure 7b.

It can be seen that the static voltage conversion ratio of the proposed converter in the charge mode has a better performance, compared with the conventional buck converter.

Discharge Mode (UC Discharge; Battery Discharge; Dual-Energy in Series Discharge)

The static voltage conversion ratio M_d in the discharge mode can be derived from the average voltage of the magnetizing inductance. According to (23) and (12), and considering the duty ratio D_d of the switch Q_1 and Q_3, the average voltage of the primary side for the coupled inductor during a switching period can be expressed as follows

$$\langle -v_{N1} \rangle_{T_s} = \int_0^{D_d T_s} (-V_L) dt + \int_{D_d T_s}^{T_s} \frac{V_H - V}{1+n} dt = 0 \tag{26}$$

The static voltage conversion ratio of the converter in the discharge mode can be derived as follows

$$M_d = \frac{V_H}{V_L} = \frac{1 + nD_d}{1 - D_d} \tag{27}$$

Figure 8a shows the relationship between the coupled inductance with different turns ratios and the static voltage conversion ratio M_d of the proposed converter in the discharge mode. For simplicity, assuming that the turns ratio of the coupling inductance is $n = 1$, the relationship between M_d and D_d is shown in Figure 8b. It can be seen that the static voltage conversion ratio of the proposed converter in the discharge mode has a better performance, compared with the conventional boost converter.

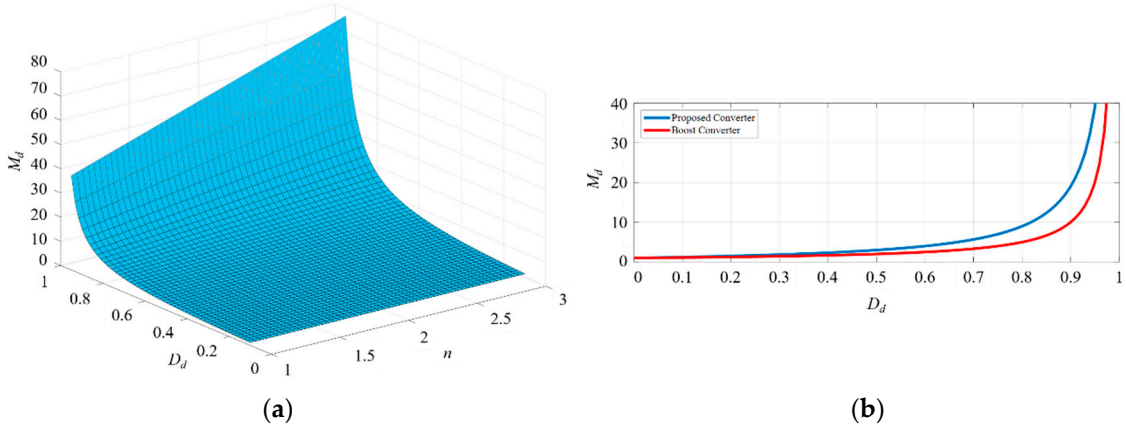

(**a**) (**b**)

Figure 8. Converter characteristics in discharge mode: (**a**) relationship diagram of M_d, D_d, and n; (**b**) relationship diagram of M_d and D_d (n = 1).

3.2. Boundary Condition Analysis

Charge Mode (UC Charge; Battery Charge)

According to the ampere-second balance principle for the filter capacitor C_L on the low-voltage side, it means that the average current of the filter capacitor should be zero in steady-state, and the sum of the averaged currents I_{T1} and I_{T2} are equal to the low-side current $I_{L,BCM}$ (i.e., UC current or battery current), as described below

$$I_{L,BCM} = \frac{V_L}{R_{L,BCM}} = I_{T1} + I_{T2} \tag{28}$$

$$I_{T1} = \frac{i_{mc1,pk}}{2(1+n)} D_c + \frac{i_{mc1,pk}}{2} (1 - D_c) \tag{29}$$

$$I_{T1} = I_{T2} = i_{mc1,pk} (1 - D_c) \tag{30}$$

In (28), $R_{L,BCM}$ represents the low-side equivalent resistance under boundary-conduction-mode (BCM) condition.

Considering the low-side voltage V_L is constant, the peak value of the magnetizing current $i_{mc1,pk}$ at BCM in the charge mode can be expressed as

$$i_{mc1,pk} = \frac{V_L}{L_m}(1 - D_c)T_s \tag{31}$$

where T_s is the switching period.

Substituting (29), (30), and (31) into (28), the boundary magnetizing inductance $L_{mc,BCM}$ in the charge mode can be derived as follows

$$L_{mc,BCM} = \frac{R_{L,BCM}(1 - D_d)}{f_s}\left[\frac{1 + n(1 - D_c)}{1 + n}\right] \tag{32}$$

The boundary time constant $\tau_{c,BCM}$ of the proposed converter in the charge mode can be derived as (33), and the corresponding relationship curve is depicted as shown in Figure 9.

$$\tau_{c,BCM} = \frac{L_{mc,BCM}f_s}{R_{L,BCM}} = (1 - D_c)\left[\frac{1 + n(1 - D_c)}{1 + n}\right] \tag{33}$$

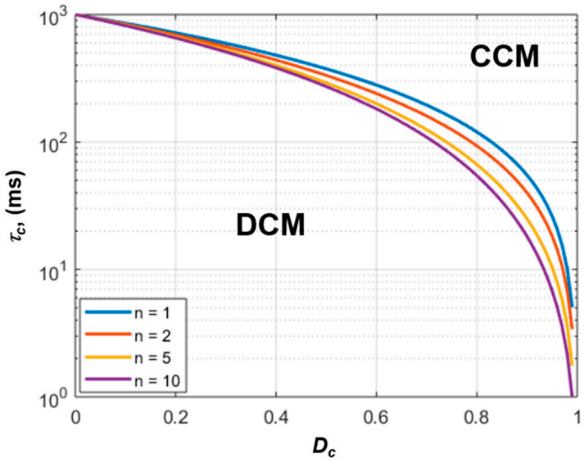

Figure 9. The curve of the boundary time constant $\tau_{c,BCM}$ in the charge mode.

Discharge Mode (UC Discharge; Battery Discharge; Dual-Energy in Series Discharge)

According to the ampere-second balance principle of the filter capacitor C_H on the high-voltage side, it can be shown that the average current on the filter capacitor is zero in steady-state, and the sum of the averaged currents I_{N2} and I_{N4} are equal to the high-side current $I_{H,BCM}$ (i.e., DC-bus current) as described below

$$I_{H,BCM} = \frac{V_H}{R_{H,BCM}} = I_{N2} + I_{N4} \tag{34}$$

$$I_{N2} = I_{N4} = \frac{i_{md1,pk}}{2(1 + n)}(1 - D_d) \tag{35}$$

where $R_{H,BCM}$ represents the high-side equivalent resistance under BCM.

Considering the high-side voltage V_H is constant, the peak value of the magnetizing current $i_{md1,pk}$ at BCM in the discharge mode can be expressed as follows

$$i_{md1,pk} = \frac{V_H T_s}{L_m}\frac{(1 - D_d)D_d}{1 + nD_d} \tag{36}$$

Substituting (35), (36) into (34) and simplifying it, the boundary magnetizing inductance in the discharge mode can be derived as follows

$$L_{md,BCM} = \frac{R_{H,BCM}}{f_s}\left[\frac{(1-D_d)^2 D_d}{(1+n)(1+nD_d)}\right] \tag{37}$$

The boundary time constant $\tau_{d,BCM}$ of the converter in the discharge mode can be derived as (38), and the corresponding relationship curve is depicted as shown in Figure 10.

$$\tau_{d,BCM} = \frac{L_{md,BCM} f_s}{R_{H,BCM}} = \frac{(1-D_d)^2 D_d}{(1+n)(1+nD_d)} \tag{38}$$

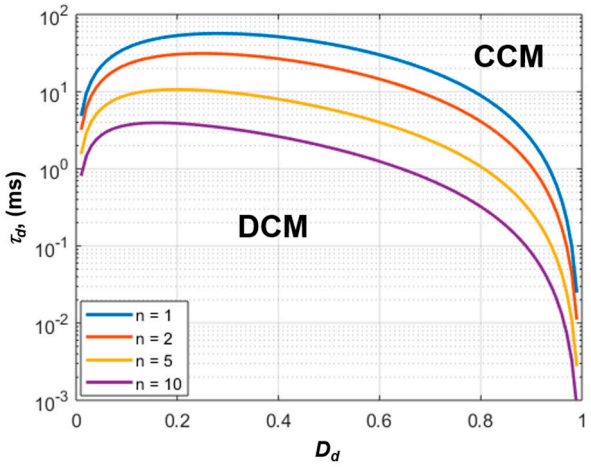

Figure 10. The curve of the boundary time constant $\tau_{d,BCM}$ in the discharge mode.

3.3. Voltage and Current Stresses Analyses of Power Devices

3.3.1. Voltage Stress Derivations

The power switching device is the main design considerations when implementing the power converter. The voltage and current stresses of the power device for the converter circuit are analyzed, and then the appropriate components are selected as below.

The multiport switches S_1~S_4 are used as the pre-stage for the discharge mode or post-stage for the charge mode. The voltage stress of the multiport switches S_1 and S_2 is equal to the UC voltage V_U, and the voltage stress of S_3 and S_4 is equal to the battery voltage V_B, as follows

$$V_{S1,\max} = V_{S2,\max} = V_U \tag{39}$$

$$V_{S3,\max} = V_{S4,\max} = V_B \tag{40}$$

The voltage stress of the power switches Q_1 to Q_4 for the converter can be expressed as follows

$$V_{Q1,\max} = V_{Q3,\max} = V_H - v_{N2} = \frac{V_H + nV_L}{1+n} \tag{41}$$

$$V_{Q2,\max} = V_{Q4,\max} = V_H - v_{N2} = V_H + nV_L \tag{42}$$

3.3.2. Current Stress Derivations

The root mean square (RMS) current of the magnetizing inductances L_{m1} and L_{m2} are derived based on the operating state of the proposed converter, as follows

$$I_{m1,rms} = I_{m2,rms} = \sqrt{{I_{m1}}^2 + \left(\frac{\Delta i_{m1}}{2\sqrt{3}}\right)^2} \tag{43}$$

where I_{m1} and I_{m2} are the DC value of the magnetizing current i_{m1} and i_{m2}, respectively; Δi_{m1} and Δi_{m2} are the magnetizing ripple currents, as follows

$$I_{m1} = I_{m2} = \frac{I_L}{2} \cdot \frac{1+n}{1+n(1-D_c)} \tag{44}$$

$$\Delta i_{m1} = \Delta i_{m2} = \frac{V_L}{L_m}(1-D_c)T_s \tag{45}$$

The RMS current of the power switches Q_1~Q_4 of the proposed converter in the charge mode can be derived as follows

$$I_{Q1,rms} = I_{Q3,rms} = I_{m1,rms}\sqrt{1-D_c} \tag{46}$$

$$I_{Q2,rms} = I_{Q4,rms} = \frac{I_{m1,rms}}{1+n}\sqrt{D_c} \tag{47}$$

The RMS current of the filter capacitors C_L and C_H of the proposed converter in the charge mode can be derived as follows

$$I_{CL,rms} = \sqrt{{I_{T1,rms}}^2 + {I_{T2,rms}}^2 - {I_L}^2} \tag{48}$$

$$I_{CH,rms} = \sqrt{{I_{Q2,rms}}^2 + {I_{Q4,rms}}^2 - {I_H}^2} \tag{49}$$

where

$$I_{T1,rms} = I_{T2,rms} = I_{m1,rms}\sqrt{\frac{D_c}{(1+n)^2} + (1-D_c)} \tag{50}$$

4. Simulated and Experimented Results

The realized converter prototype is shown in Figure 11, and Table 1 shows the electrical specifications and the circuit parameters of the realized power converter. For the convenience of the experiments, in the charge mode, the power supply (ITECH IT6726G) was used as the DC-bus on the high-voltage side, and the electronic load (ITECH IT8814B) was used as the UC or the battery on the low-voltage side. Conversely, in the discharge mode, the power supply was used as the UC, the battery, or the dual-energy storage in series.

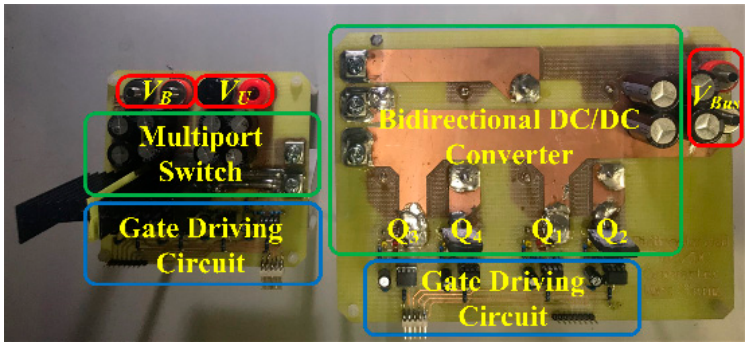

Figure 11. Prototype circuit of the proposed converter.

Table 1. Specifications and circuit parameters of the realized power converter.

Symbol	Descriptions	Specifications
V_H (V_{bus})	high-side voltage (DC-bus voltage)	72 V
V_L	low-side voltage	
V_B	battery voltage	20 V~26 V
V_U	UC voltage	0 V~48 V
P_o	rated output power	500 W
f_s	switching frequency	20 kHz
Symbol	**Descriptions**	**Parameters**
L_{m1}, L_{m2}	magnetizing inductances of the coupled inductors	250 μH
n	turns ratio of the coupled inductors	1
C_H	high-side capacitor	2400 μF
C_L	low-side capacitor	800 μF

UC Charge Mode

Figures 12 and 13 show the waveforms of the gate signals of Q_2 and Q_4, the primary-side currents of the coupled inductor (i_{T1}, i_{T2}), the secondary-side currents of the coupled inductor (i_{N2}, i_{N4}), and the low-side voltage V_U in the UC charge mode with full load condition, respectively. In this mode, the UC voltage was about 48 V, the duty ratio of the switches Q_2 and Q_4 was set to 80% (i.e., D_c = 0.8), the DC values of the primary currents (i_{T1}, i_{T2}) and secondary currents (i_{N2}, i_{N4}) of the coupled inductance were about 5.2 A and 3.5 A, respectively.

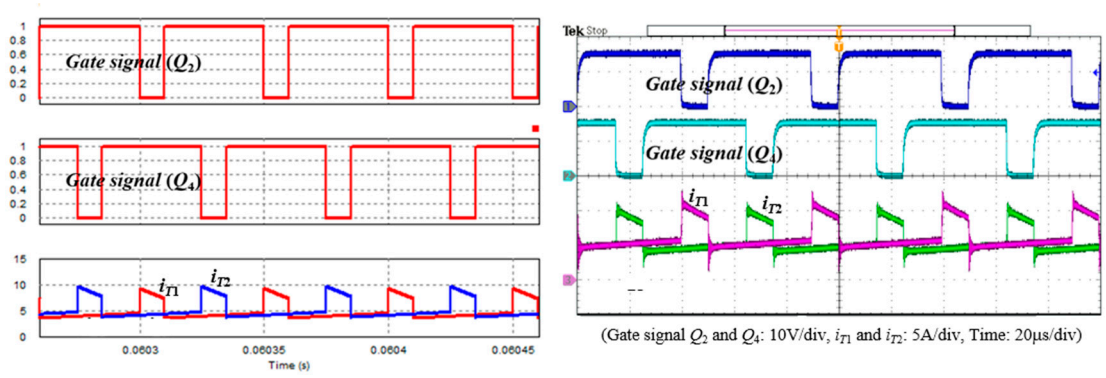

(**a**) (**b**)

Figure 12. Waveforms of the switching gate signals and the primary-side currents of the coupled inductor in the UC recharging mode with D_c = 0.8: (**a**) simulated and (**b**) experimental.

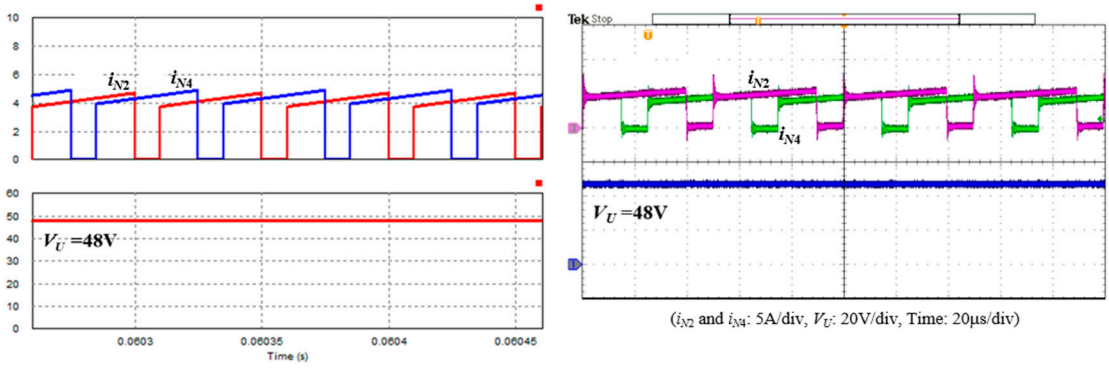

(**a**) (**b**)

Figure 13. The waveform of the secondary-side currents of the coupled inductor and UC voltage in the UC charge mode with D_c = 0.8: (**a**) simulated and (**b**) experimental.

Figure 14 shows the waveforms of the steady-state switching voltages across the power devices in the UC charge mode. The results showed that the steady-state switching voltages across the lower-leg MOSFETs Q_1 and Q_3 were about 60 V, and the steady-state switching voltages across the upper-leg MOSFETs Q_2 and Q_4 were about 120 V. It could be seen that in Figure 14, the simulation and the experimental results were consistent and corresponded to (41) and (42).

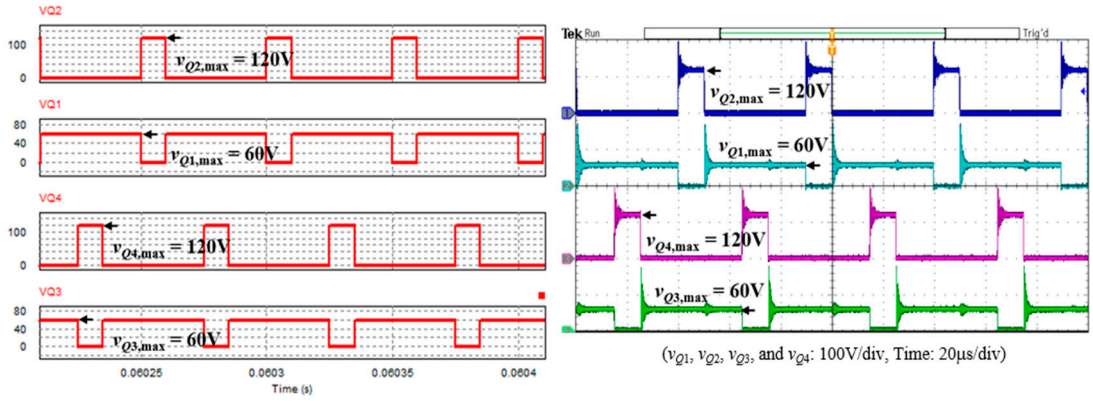

(**a**) (**b**)

Figure 14. The waveform of switching voltage across the power devices in the UC charge mode with D_c = 0.8: (**a**) simulated and (**b**) experimental.

Battery Charge Mode

Figures 15 and 16 show the waveforms of the gate signals of Q_2 and Q_4, the primary-side currents of the coupled inductor (i_{T1}, i_{T2}), the secondary-side currents of the coupled inductor (i_{N2}, i_{N4}), and the low-side voltage V_{LI} in the battery charge mode with full load condition, respectively.

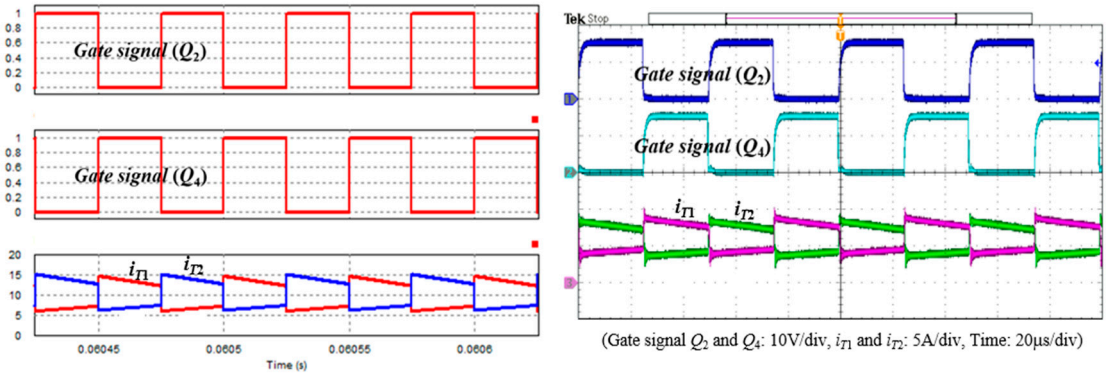

(**a**) (**b**)

Figure 15. Waveforms of the switching gate signals and the primary-side currents of the coupled inductor in the battery charge mode with D_c = 0.5: (**a**) simulated and (**b**) experimental.

In this mode, the battery voltage was about 24 V, the duty ratio of the switches Q_2 and Q_4 was set to 50% (i.e., D_c = 0.5), and the DC values of the primary currents (i_{T1}, i_{T2}) and secondary currents (i_{N2}, i_{N4}) of the coupled inductance were about 10.4 A and 3.5 A, respectively. It could be seen that in Figures 15 and 16, the simulation and the experimental results were consistent.

Figure 17 shows the waveforms of the steady-state switching voltages across the power devices in the battery charge mode. The results showed that the steady-state switching voltages across the lower-leg MOSFETs Q_1 and Q_3 were about 48 V, and the steady-state switching voltages across the

upper-leg MOSFETs Q_2 and Q_4 were about 96 V. It could be seen that in Figure 17, the simulation and the experimental results were consistent and corresponded to (41) and (42).

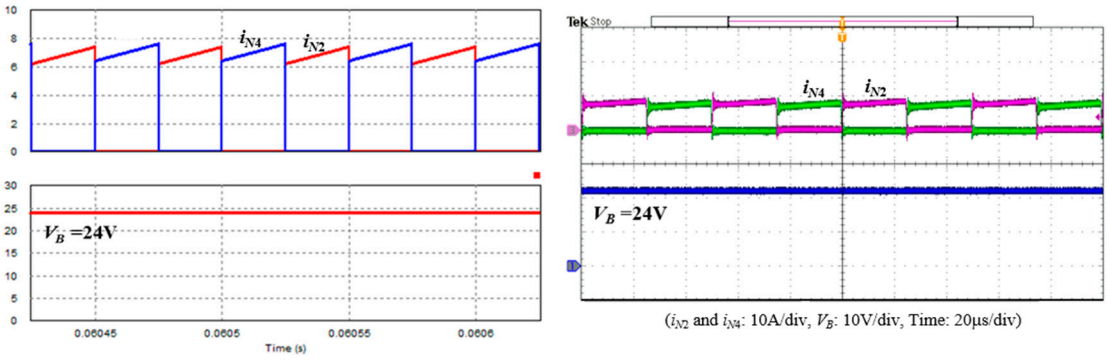

(**a**) (**b**)

Figure 16. The waveform of the secondary-side currents of the coupled inductor and UC voltage in the battery charge mode with D_c = 0.5: (**a**) simulated and (**b**) experimental.

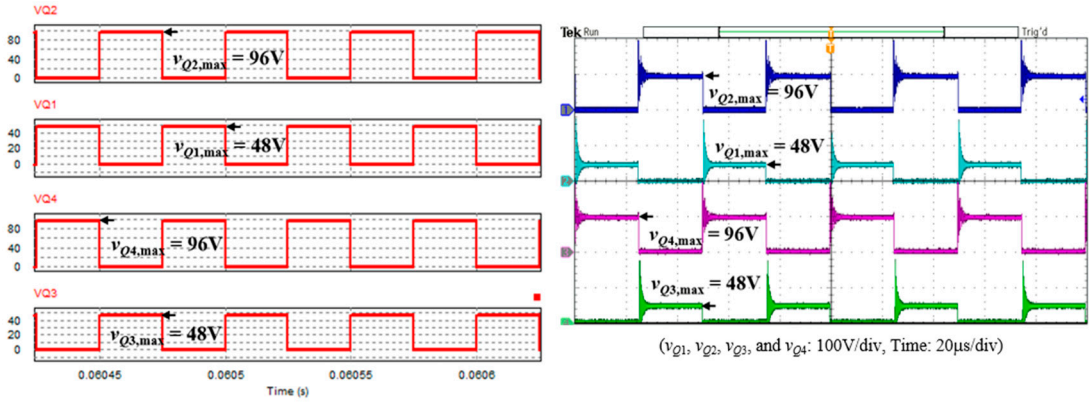

(**a**) (**b**)

Figure 17. The waveform of switching voltage across the power devices in the battery charge mode with D_c = 0.5: (**a**) simulated and (**b**) experimental.

UC Discharge Mode

Figures 18 and 19 show the waveforms of the gate signals of Q_2 and Q_4, the primary-side currents of the coupled inductor (i_{T1}, i_{T2}), the secondary-side currents of the coupled inductor (i_{N2}, i_{N4}), and the high-side voltage V_H in the UC discharge mode with full load condition, respectively.

In this mode, the DC-bus voltage was about 72 V, the duty ratio of the switches Q_1 and Q_3 was set to 20% (i.e., D_d = 0.2), and the DC values of the primary currents (i_{T1}, i_{T2}) and secondary currents (i_{N2}, i_{N4}) of the coupled inductance were about 5.2 A and 3.5 A, respectively. It could be seen that in Figures 18 and 19, the simulation and the experimental results were consistent.

Figure 20 shows the waveforms of the steady-state switching voltages across the power devices in the UC discharge mode. The results showed that the steady-state switching voltages across the lower-leg MOSFETs Q_1 and Q_3 were about 60 V, and the steady-state switching voltages across the upper-leg MOSFETs Q_2 and Q_4 were about 120 V. It could be seen that in Figure 20, the simulation and the experimental results were consistent and corresponded to (41) and (42).

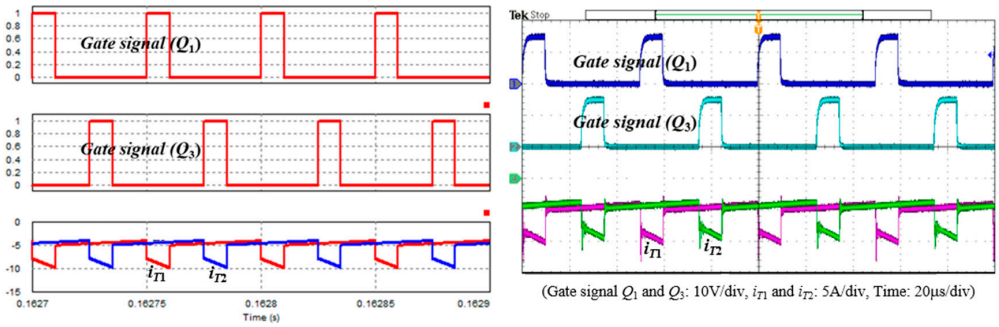

(**a**) (**b**)

Figure 18. Waveforms of the switching gate signals and the primary-side currents of the coupled inductor in the UC discharging mode with D_d = 0.2: (**a**) simulated and (**b**) experimental.

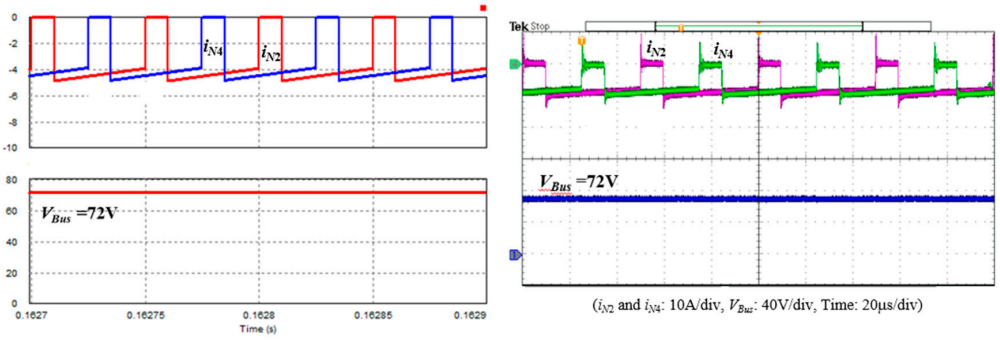

(**a**) (**b**)

Figure 19. The waveform of the secondary-side currents of the coupled inductor and DC-bus voltage in the UC discharging mode with D_d = 0.2: (**a**) simulated and (**b**) experimental.

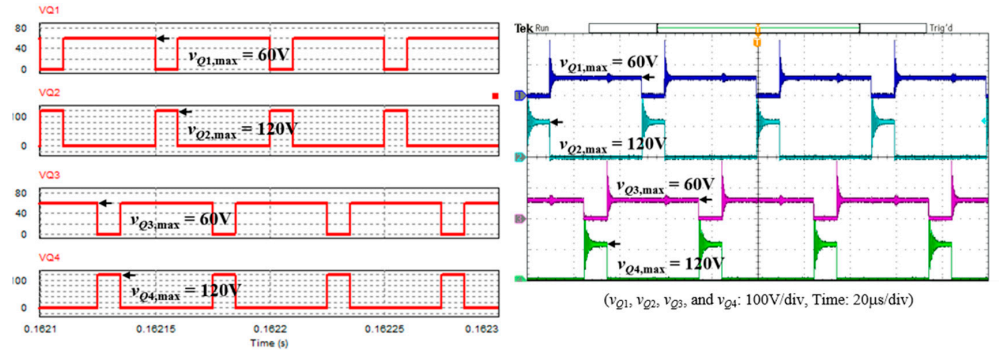

(**a**) (**b**)

Figure 20. The waveform of switching voltage across the power devices in the UC discharging mode with D_d = 0.2: (**a**) simulated and (**b**) experimental.

Dual-Energy in Series Discharge Mode

Figures 21 and 22 show the waveforms of the gate signals of Q_2 and Q_4, the primary-side currents of the coupled inductor (i_{T1}, i_{T2}), the secondary-side currents of the coupled inductor (i_{N2}, i_{N4}), and the high-side voltage V_H in the dual-energy discharge mode with full load condition, respectively.

In this mode, the DC-bus voltage was about 72 V, the low-side voltage V_L was 44 V, the duty ratio of the switches Q_1 and Q_3 was set to 25% (i.e., D_d = 0.25), and the DC values of the primary currents (i_{T1}, i_{T2}) and secondary currents (i_{N2}, i_{N4}) of the coupled inductance were about 5.8 A and 3.5 A, respectively. It could be seen that in Figures 21 and 22, the simulation and the experimental results were consistent.

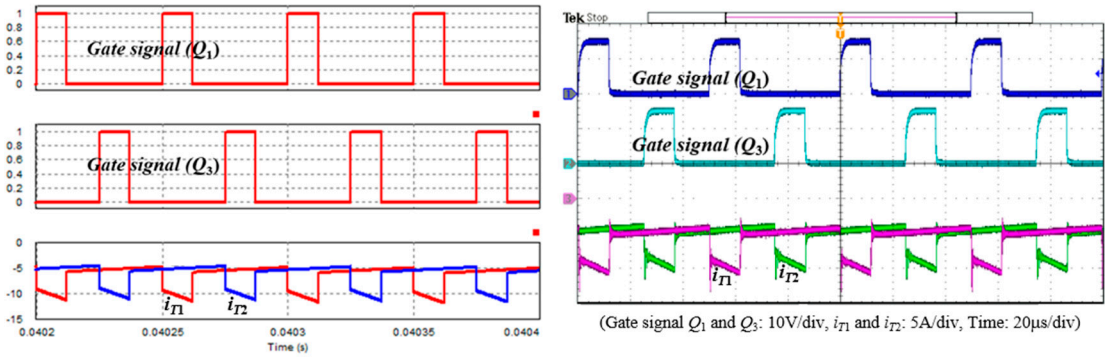

(**a**) (**b**)

Figure 21. Waveforms of the switching gate signals and the primary-side currents of the coupled inductor in the dual-energy in series discharge mode with $D_d = 0.25$: (**a**) simulated and (**b**) experimental.

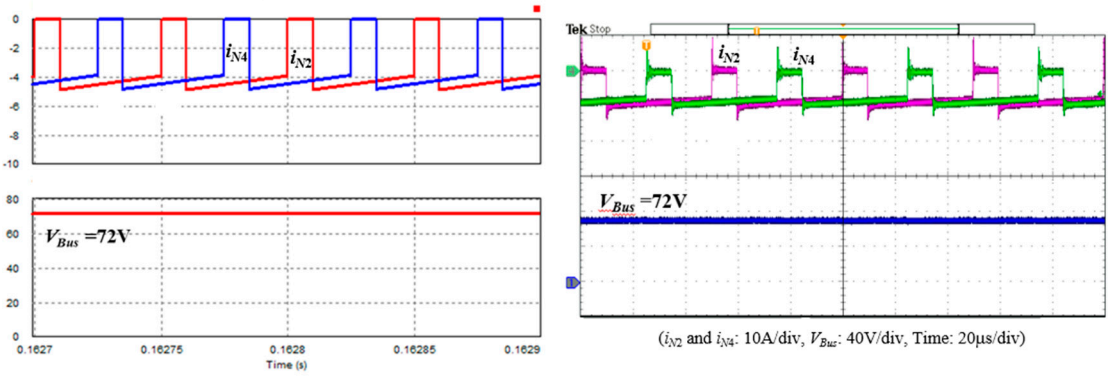

(**a**) (**b**)

Figure 22. The waveform of the secondary-side currents of the coupled inductor and DC-bus voltage in the dual-energy in series discharge mode with $D_d = 0.25$: (**a**) simulated and (**b**) experimental.

Figure 23 shows the waveforms of the steady-state switching voltages across the power devices in the dual-energy in series discharge mode. The results showed that the steady-state switching voltages across the lower-leg MOSFETs Q_1 and Q_3 were about 58 V, and the steady-state switching voltages across the upper-leg MOSFETs Q_2 and Q_4 were about 116 V. It could be seen that in Figure 23, the simulation and the experimental results were consistent and corresponded to (41) and (42).

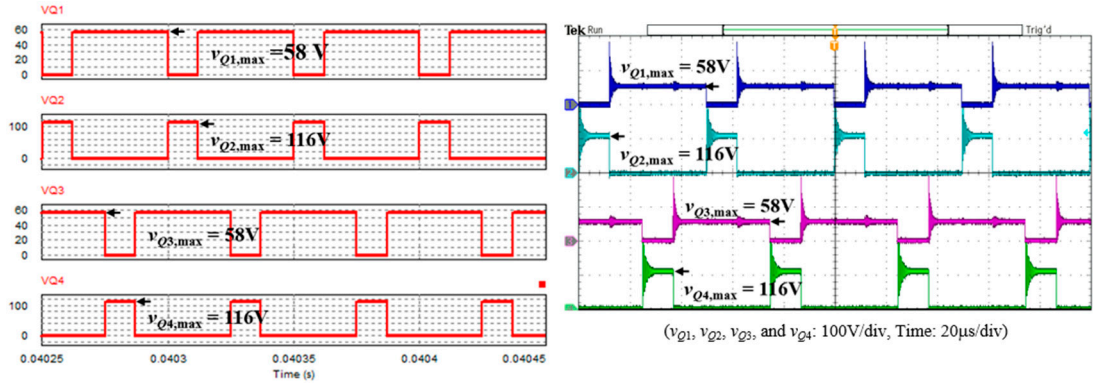

(**a**) (**b**)

Figure 23. The waveform of switching voltage across the power devices in the dual-energy in series discharge mode with $D_d = 0.25$: (**a**) simulated and (**b**) experimental.

Efficiency Measurement

The system used two power analyzers (YOKOGAWA WT310) connected to the input and output of the realized converter prototype. As could be seen in Figure 24, in the UC charge mode, the highest efficiency point was 97.4%; in the battery charge mode, the highest efficiency point was 95.5%; in the UC discharge mode, the highest efficiency point was 97.2%; in the dual-energy in series discharge mode, the highest efficiency point was 97.1%; in the battery discharge mode, the highest efficiency point was 95.3%.

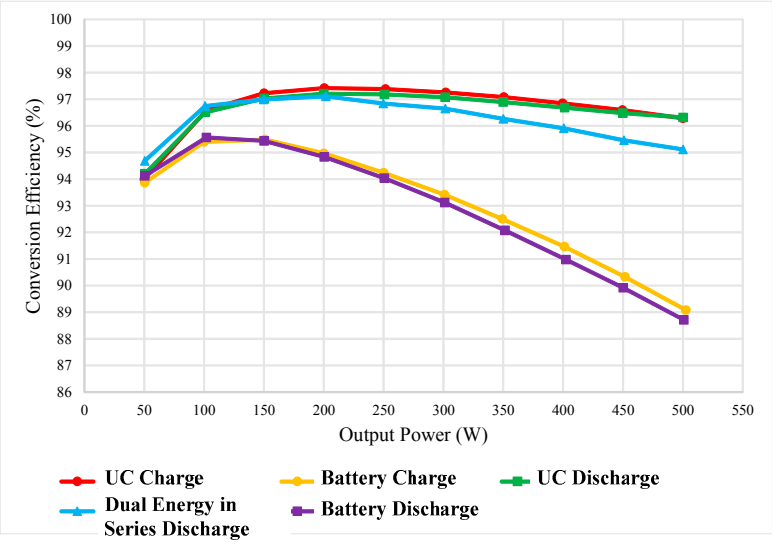

Figure 24. The measured efficiency of the proposed converter for the different operating modes.

5. Conclusions

This study proposed a patented bidirectional power converter that used dual-energy storage as input sources and incorporated a coupled inductor to obtain a higher voltage conversion ratio. The converter control used IPWM control to achieve low current ripple, dissipate low side current stress, and reduce the conduction loss of the power MOSFET. Moreover, the proposed bidirectional power converter in this study also discussed the steady-state operation in the charge mode and discharge mode, respectively. The voltage conversion ratio, boundary conditions, and voltage and current stress of each power component of the converter were analyzed. Finally, this study implemented a converter prototype with a 500 W power rating for verification. The simulation results and the experimental results were consistent; the highest efficiency points of the realized prototype were 97.4%, 95.5%, 97.2%, 97.1%, and 95.3% for the UC charge mode, battery charge mode, UC discharge mode, the dual-energy in series discharge mode, and battery discharge mode, respectively. In summary, this paper demonstrated that the proposed bidirectional power converter could be potentially applied to produce hybrid power architecture (has been patented [37]).

Author Contributions: C.-M.L. substantially contributed to the examination and interpretation of the results, development of the overall system, and review and proofreading of the manuscript. J.T. and Y.L. substantially contributed to the review and proofreading of the manuscript. Y.-C.L. substantially contributed to literature search, control strategy design, and production and analysis of the results. All authors have read and agreed to the published version of the manuscript.

Funding: This work was supported in part by the Ministry of Science and Technology (MOST), Taiwan, R.O.C., under grant MOST-107-2221-E-005-079-MY3, MOST-107-2221-E-005-080-MY2, MOST-108-2218-E-005-021, and MOST-108-2638-E-005-001-MY2.

Acknowledgments: The authors would like to express their appreciation to the Chih-Yu Yang (guided by Prof. Ching-Ming Lai) for the experimental bench setup.

Conflicts of Interest: The authors declare no conflict of interest.

Nomenclature

T_1, T_2	Two-phase coupled inductors
L_{m1}, L_{m2}	Magnetizing inductors of the two-phase coupled inductors
$L_{mc,BCM}$	Boundary magnetizing inductance in the charge mode
$L_{md,BCM}$	Boundary magnetizing inductance in the discharge mode
n	Turns ratio of the two-phase coupled inductors ($n = N_2/N_1 = N_4/N_3$)
N_1	Primary winding of T_1
N_2	Secondary winding of T_1
N_3	Primary winding of T_2
N_4	Secondary winding of T_2
k	Coupling coefficient
C_U	Input capacitor paralleled with UC
C_B	Input capacitor paralleled with BES
S_1~S_4	Power devices of the multiport switch
Q_1~Q_4	Power devices of the two-phase bidirectional power converter
V_H	High-side voltage for the DC-bus
V_L	Low-side voltage for UC, BES, or BES/UC dual-energy in series
V_U	UC voltage
V_B	BES voltage
i_{Bus}	DC-bus current
i_{Uc}	UC current
i_{Bat}	BES current
i_H	High voltage side current
i_L	Low voltage side current
$I_{L,BCM}$	Low voltage side current under BCM condition
$I_{H,BCM}$	High voltage side current under BCM condition
$I_{m1,rms}$, $I_{m2,rms}$	RMS value of the magnetizing currents of the coupled inductors
$I_{T1,rms}$, $I_{T2,rms}$	RMS value of the primary-side currents of the coupled inductors
v_{N1}	Voltage of the winding N_1 of the T_1
v_{N2}	Voltage of the winding N_2 of the T_1
v_{N3}	Voltage of the winding N_3 of the T_2
v_{N4}	Voltage of the winding N_4 of the T_2
$V_{S1,\max}$~$V_{S4,\max}$	Switch voltage stress of the multiport switch
$V_{Q1,\max}$~$V_{Q4,\max}$	Switch voltage stress of the two-phase bidirectional power converter
i_{T1}, i_{T2}	The primary-side currents of the two-phase coupled inductors
i_T	The sum of the primary-side currents i_{T1} and i_{T2}
i_{N2}, i_{N4}	The secondary-side currents of the two-phase coupled inductors
i_{m1}, i_{m2}	Magnetizing inductor currents of the coupled inductors T_1 and T_2
I_{m1}, I_{m2}	DC value of the magnetizing currents
$i_{mc,pk}$	peak value of the magnetizing inductor current under BCM in the charge mode
$i_{md,pk}$	peak value of the magnetizing inductor current under BCM in the discharge mode
Δi_{m1}, Δi_{m2}	Magnetizing ripple currents
$I_{Q1,\mathrm{rms}}$~$I_{Q4,\mathrm{rms}}$	RMS current of the power switches Q_1~Q_4
$I_{CH,\mathrm{rms}}$~$I_{CL,\mathrm{rms}}$	RMS current of the filter capacitors C_L and C_H
D_c, D_d	Duty ratio of charge mode and discharge mode
T_s	Switching period
$\tau_{c,BCM}$	Boundary time constant in the charge mode
$\tau_{d,BCM}$	Boundary time constant in the discharge mode
$R_{L,BCM}$	Low-side equivalent resistance under BCM condition
$R_{H,BCM}$	High-side equivalent resistance under BCM condition
M_c	Static voltage conversion ratio in the charge mode
M_d	Static voltage conversion ratio in the discharge mode

References

1. Lai, J.S.; Nelson, D.J. Energy management power converters in hybrid electric and fuel cell vehicles. *Proc. IEEE* **2007**, *95*, 766–777. [CrossRef]
2. Bauman, J.; Kazerani, M. A comparative study of fuel-cell-battery, fuel-cell-ultracapacitor, and fuel-cell-battery-ultracapacitor vehicles. *IEEE Trans. Veh. Technol.* **2008**, *57*, 760–769. [CrossRef]
3. Khaligh, A.; Li, Z. Battery ultracapacitor fuel cell and hybrid energy storage systems for electric hybrid electric fuel cell and plug-in hybrid electric vehicles: State of the art. *IEEE Trans. Veh. Technol.* **2010**, *59*, 2806–2814. [CrossRef]
4. Chan, C.C.; Bouscayrol, A.; Chen, K. Electric, hybrid, and fuel-cell vehicles: Architectures and modeling. *IEEE Trans. Veh. Technol.* **2010**, *59*, 589–598. [CrossRef]
5. Rajashekara, K. Present status and future trends in electric vehicle propulsion technologies. *IEEE J. Emerg. Sel. Top. Power Electron.* **2013**, *1*, 3–10. [CrossRef]
6. Zhang, Y.; Meng, D.; Zhou, M.; Li, S. Energy management of an electric city bus with battery/ultra-capacitor HESS. In Proceedings of the 2016 IEEE Vehicle Power and Propulsion Conference (VPPC), Hangzhou, China, 17–20 October 2016.
7. Cheng, Y.H.; Lai, C.M. Control strategy optimization for parallel hybrid electric vehicles using memetic algorithm. *Energies* **2017**, *10*, 305. [CrossRef]
8. Cheng, L.; Acuna, P.; Aguilera, R.P.; Jiang, J.; Flecther, J.; Baier, C. Model predictive control for energy management of a hybrid energy storage system in light rail vehicles. In Proceedings of the 2017 11th IEEE International Conference on Compatibility, Power Electronics and Power Engineering (CPE-POWERENG), Cadiz, Spain, 4–6 April 2017; pp. 683–688.
9. Un-Noor, F.; Padmanaban, S.; Mihet-Popa, L.; Mollah, M.N.; Hossain, E.A. Comprehensive study of key electric vehicle (EV) components, technologies, challenges, impacts, and future direction of development. *Energies* **2017**, *10*, 1217. [CrossRef]
10. Serpi, A.; Porru, M. Modelling and design of real-time energy management systems for fuel cell/battery electric vehicles. *Energies* **2019**, *12*, 4260. [CrossRef]
11. Schaltz, E.; Khaligh, A.; Rasmussen, P.O. Influence of battery/ultracapacitor energy-storage sizing on battery lifetime in a fuel cell hybrid electric vehicle. *IEEE Trans. Veh. Technol.* **2009**, *58*, 3882–3891. [CrossRef]
12. Cao, J.; Emadi, A. A new battery/ultracapacitor hybrid energy storage system for electric, hybrid, and plug-in hybrid electric vehicles. *IEEE Trans. Power Electron.* **2012**, *27*, 122–132.
13. Momayyezan, M.; Hredzak, B.; Agelidis, V.G. A new multiple converter topology for battery/ultracapacitor hybrid energy system. In Proceedings of the Annual Conference of the IEEE Industrial Electronics Society, Yokohama, Japan, 9–12 November 2015; pp. 464–468.
14. Juned, S.; Mohammad, S.; Bhanabhagvanwala, D. Simulation analysis of battery/ultracapacitor hybrid energy storage system for electric vehicle. In Proceedings of the International Conference on Intelligent Sustainable Systems, Palladam, India, 21–22 February 2019.
15. Chakraborty, S.; Vu, H.-N.; Hasan, M.M.; Tran, D.-D.; Baghdadi, M.E.; Hegazy, O. DC-DC converter topologies for electric vehicles, plug-in hybrid electric vehicles and fast charging stations: State of the art and future trends. *Energies* **2019**, *12*, 1569. [CrossRef]
16. Ding, S.; Wei, B.; Hang, J.; Zhang, P.; Ding, M. *A Multifunctional Interface Circuit for Battery-Ultracapacitor Hybrid Energy Storage System*; NSW: Sydney, Australia, 2017.
17. Ortúzar, M.; Moreno, J.; Dixon, J. Ultracapacitor-based auxiliary energy system for an electric vehicle: Implementation and evaluation. *IEEE Trans. Ind. Electron.* **2007**, *54*, 2147–2156. [CrossRef]
18. Machado, F.; Antunes, C.H.; Dubois, M.R.; Trovao, J.P. Semi-active hybrid topology with three-level DC-DC converter for electric vehicle application. In Proceedings of the 2015 IEEE Vehicle Power and Propulsion Conference (VPPC), Montreal, QC, Canada, 19–22 October 2015; pp. 1–6.
19. Shen, J.; Khaligh, A. A supervisory energy management control strategy in a battery/ultracapacitor hybrid energy storage system. *IEEE Trans. Transp. Electrif.* **2015**, *1*, 223–231. [CrossRef]
20. Castaings, A.; Lhomme, W.; Trigui, R.; Bouscayrol, A. Practical control schemes of a battery/supercapacitor system for electric vehicle. *IET Electr. Syst. Transp.* **2016**, *6*, 20–26. [CrossRef]
21. Kuperman, A.; Aharon, I.; Malki, S.; Kara, A. Design of a semiactive battery-ultracapacitor hybrid energy source. *IEEE Trans. Power Electron.* **2013**, *28*, 806–815. [CrossRef]

22. Onar, O.; Khaligh, A. Dynamic modeling and control of a cascaded active battery/ultra-capacitor based vehicular power system. In Proceedings of the 2008 IEEE Vehicle Power and Propulsion Conference (VPPC), Harbin, China, 3–5 September 2008.
23. Jing, W.; Lai, C.H.; Wong, S.H.W.; Wong, M.L.D. Battery-supercapacitor hybrid energy storage system in standalone DC microgrids: Areview. *IET Renew. Power Gener.* **2017**, *11*, 461–469. [CrossRef]
24. Allegre, A.L.; Bouscayrol, A.; Trigui, R. Flexible real-time control of a hybrid energy storage system for electric vehicles. *IET Electr. Syst. Transp.* **2013**, *3*, 79–85. [CrossRef]
25. Trovão, J.P.F.; Pereirinha, P.G. Control scheme for hybridised electric vehicles with an online power follower management strategy. *IET Electr. Syst. Transp.* **2015**, *5*, 12–23. [CrossRef]
26. Trovao, J.P.; Silva, M.A.; Dubois, M.R. Coupled energy management algorithm for MESS in urban EV. *IET Electr. Syst. Transp.* **2017**, *7*, 125–134. [CrossRef]
27. Livreri, P.; Castiglia, V.; Pellitteri, F.; Miceli, R. Design of a battery/ultracapacitor energy storage system for electric vehicle applications. In Proceedings of the IEEE International Forum on Research and Technologies for Society and Industry, Palermo, Italy, 10–13 September 2018; pp. 1–5.
28. Lu, X.; Wang, H. Optimal sizing and energy management for cost-effective PEV hybrid energy storage systems. *IEEE Trans. Ind. Inform.* **2020**, *16*, 3407–3416. [CrossRef]
29. Gummi, K.; Ferdowsi, M. Double-input DC–DC power electronic converters for electric-drive vehicles-Topology exploration and synthesis using a single-pole triple-throw switch. *IEEE Trans. Ind. Electron.* **2010**, *57*, 617–623. [CrossRef]
30. Kumar, L.; Jain, S. Multiple-input DC/DC converter topology for hybrid energy system. *IET Power Electron.* **2013**, *6*, 1483–1501. [CrossRef]
31. Lai, C.M.; Yang, M.J. A high-gain three-port power converter with fuel cell, battery sources and stacked output for hybrid electric vehicles and DC-microgrids. *Energies* **2016**, *9*, 180. [CrossRef]
32. Hintz, A.; Prasanna, U.R.; Rajashekara, K. Novel modular multiple-input bidirectional DC-DC power converter (MIPC) for HEV/FCV application. *IEEE Trans. Ind. Electron.* **2015**, *62*, 3163–3172. [CrossRef]
33. Lai, C.M.; Cheng, Y.H.; Hsieh, M.H.; Lin, Y.C. Development of a bidirectional DC/DC converter with dual-battery energy storage for hybrid electric vehicle system. *IEEE Trans. Veh. Technol.* **2018**, *67*, 1036–1052. [CrossRef]
34. Hernándeza, J.C.; Ruiz-Rodriguezb, F.J.; Juradoc, F. Modelling and assessment of the combined technical impact of electric vehicles and photovoltaic generation in radial distribution systems. *Energy* **2017**, *141*, 316–332. [CrossRef]
35. Hernándeza, J.C.; Sanchez-Sutila, F.; Muñoz-Rodríguezb, F.J. Design criteria for the optimal sizing of a hybrid energy storage system in PV household-prosumers to maximize self-consumption and self-sufficiency. *Energy* **2019**, *186*, 115827. [CrossRef]
36. Gomez-Gonzaleza, M.; Hernandezb, J.C.; Veraa, D.; Juradoa, F. Optimal sizing and power schedule in PV household-prosumers for improving PV self-consumption and providing frequency containment reserve. *Energy* **2020**, *191*, 116554. [CrossRef]
37. Lai, C.-M.; Yang, C.-Y.; Cheng, Y.-H. Power Supply System and Power Supply Method for Electric Vehicle. Taiwan Patent No. I642575, 1 December 2018.